

Spatial and temporal distribution of mass loss from the Greenland Ice Sheet since AD 1900

Kristian K. Kjeldsen^{1,2*}, Niels J. Korsgaard^{1*}, Anders A. Bjørk¹, Shfaqat A. Khan³, Jason E. Box⁴, Svend Funder¹, Nicolaj K. Larsen^{1,5}, Jonathan L. Bamber⁶, William Colgan^{4,7}, Michiel van den Broeke⁸, Marie-Louise Siggaard-Andersen¹, Christopher Nuth⁹, Anders Schomacker¹, Camilla S. Andresen⁴, Eske Willerslev¹ & Kurt H. Kjær¹

The response of the Greenland Ice Sheet (GIS) to changes in temperature during the twentieth century remains contentious¹, largely owing to difficulties in estimating the spatial and temporal distribution of ice mass changes before 1992, when Greenland-wide observations first became available². The only previous estimates of change during the twentieth century are based on empirical modelling^{3–5} and energy balance modelling^{6,7}. Consequently, no observation-based estimates of the contribution from the GIS to the global-mean sea level budget before 1990 are included in the Fifth Assessment Report of the Intergovernmental Panel on Climate Change⁸. Here we calculate spatial ice mass loss around the entire GIS from 1900 to the present using aerial imagery from the 1980s. This allows accurate high-resolution mapping of geomorphic features related to the maximum extent of the GIS during the Little Ice Age⁹ at the end of the nineteenth century. We estimate the total ice mass loss and its spatial distribution for three periods: 1900–1983 (75.1 ± 29.4 gigatonnes per year), 1983–2003 (73.8 ± 40.5 gigatonnes per year), and 2003–2010 (186.4 ± 18.9 gigatonnes per year). Furthermore, using two surface mass balance models^{10,11} we partition the mass balance into a term for surface mass balance (that is, total precipitation minus total sublimation minus runoff) and a dynamic term. We find that many areas currently undergoing change are identical to those that experienced considerable thinning throughout the twentieth century. We also reveal that the surface mass balance term shows a considerable decrease since 2003, whereas the dynamic term is constant over the past 110 years. Overall, our observation-based findings show that during the twentieth century the GIS contributed at least 25.0 ± 9.4 millimetres of global-mean sea level rise. Our result will help to close the twentieth-century sea level budget, which remains crucial for evaluating the reliability of models used to predict global sea level rise^{1,8}.

We use aerial stereo photogrammetric imagery recorded during the period 1978–1987 to map trimlines and lateral and end moraines associated with the maximum extent of the GIS during the Little Ice Age (LIA_{max}), thereby quantifying vertical changes in ice surface elevation between the LIA_{max} and 1978–87 (Fig. 1, Methods). To obtain a rate of ice mass loss, the year 1900 AD is assigned as a Greenland-wide time stamp of when the glaciers started to retreat from their LIA_{max} position (although we note that this varies regionally and locally^{9,12,13}), and 1983 is assigned as the mean year of the aerial observations. Elevation differences after 1983 are derived from airborne and satellite altimetry, combined with a digital elevation model (DEM) developed from the aerial imagery (Methods). We use this geodetic approach to calculate spatially distributed ice thinning patterns and mass balance of the GIS

for three periods (Fig. 2a–c); LIA_{max}(1900) to 1983, 1983 to 2003, and 2003 to 2010. We omitted some areas of the GIS because of the lack of LIA data points (Methods).

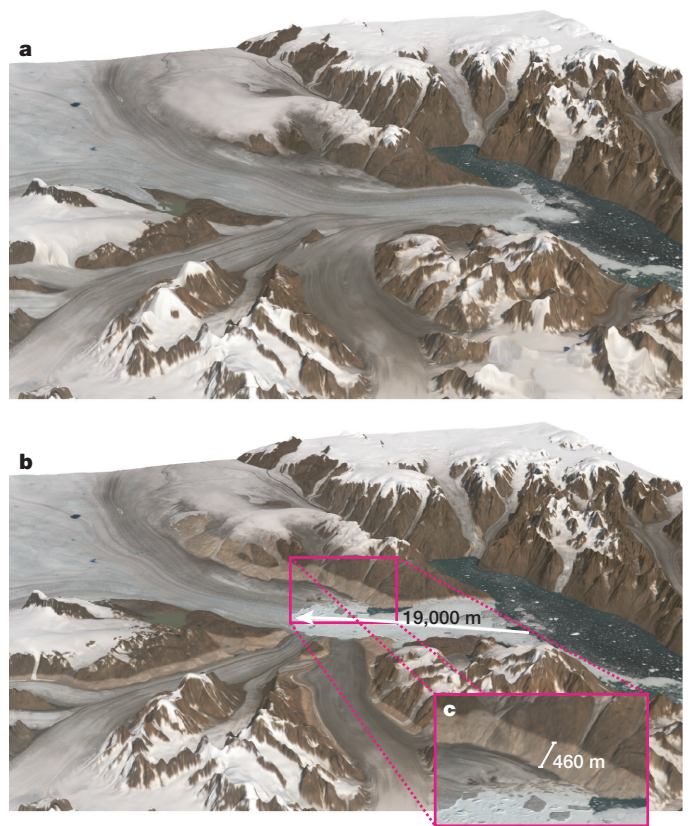


Figure 1 | Three-dimensional models of Kangerlussuaq Glacier.

a, Reconstruction of the LIA_{max} ice surface at 1900. **b**, The 2013 ice surface. **c**, Close-up of the northern rim of the 2013 ice surface. The base map is Landsat 8 satellite imagery from 2013. The LIA marks a cold period during which the GIS expanded, often associated with the time interval from 1450–1850²⁹. A spectacular indication that the GIS has been shrinking over the last century are the fresh trimlines, that is, the pronounced boundaries between abraded and less abraded bedrock on valley sides and fresh non-vegetated moraines close to the present glacier fronts in many areas of Greenland. Both features are considered to mark the culmination of LIA-glacial advances and to have been mainly formed during the 1700s or at the end of the 1800s³⁰.

¹Centre for GeoGenetics, Natural History Museum, University of Copenhagen, Copenhagen 1350, Denmark. ²Department of Earth Sciences, University of Ottawa, Ottawa, Ontario K1N 6N5, Canada.

³DTU Space—National Space Institute, Technical University of Denmark, Department of Geodesy, Kongens Lyngby 2800, Denmark. ⁴Geological Survey of Denmark and Greenland, Department of Marine Geology and Glaciology, Copenhagen 1350, Denmark. ⁵Department of Geoscience, Aarhus University, Aarhus 8000, Denmark. ⁶Bristol Glaciology Centre, University of Bristol, Bristol BS8 1SS, UK. ⁷Department of Earth and Space Science and Engineering, York University, Toronto, Ontario M3J 1P3, Canada. ⁸Institute for Marine and Atmospheric Research, Utrecht University, Utrecht 80005, The Netherlands. ⁹Department of Geosciences, University of Oslo, Oslo 0316, Norway.

*These authors contributed equally to this work.

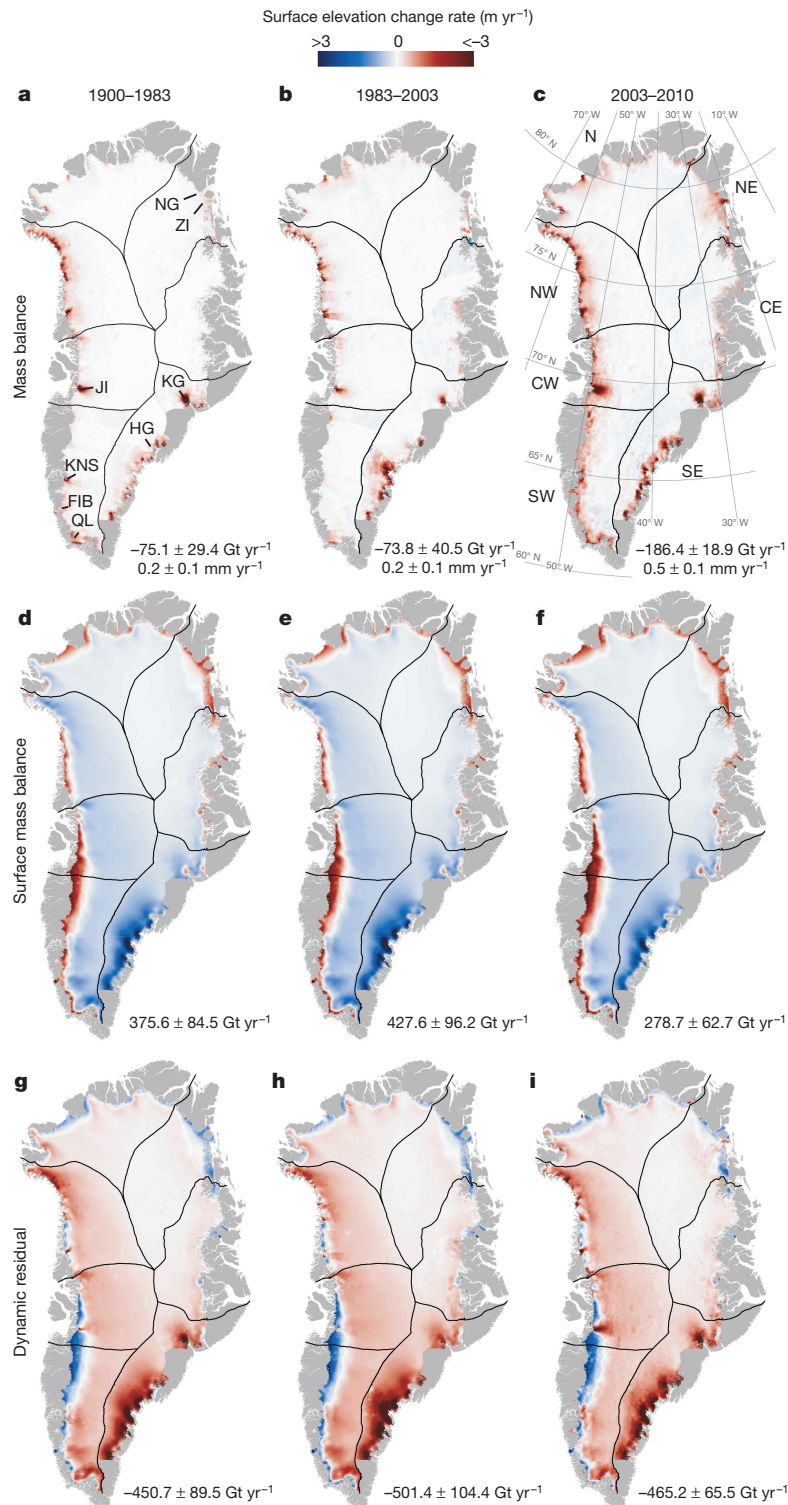


Figure 2 | Surface elevation change rates in Greenland since the LIA maximum. The colour scale applies to all panels. **a–c**, Estimates of surface elevation change rates during LIA_{max}(1900)–1983 (**a**), 1983–2003 (**b**) and 2003–2010 (**c**). The numbers listed below each panel are the integrated Greenland-wide mass balance estimates expressed as gigatonnes per year and as millimetre per year GMSL equivalents. The associated uncertainties include an uncertainty related to the scaling approach, an error related to observed changes during 2003–2010, and an uncertainty related to the scaling of the point-based observations. **d–f**, Total estimates of surface elevation change rates due to SMB fluctuations, using revised SMB

estimates from ref. 10 during LIA_{max}(1900)–1983 (**d**), 1983–2003 (**e**), and 2003–2010 (**f**). **g–i**, The dynamically driven residual in elevation change rates during LIA_{max}(1900)–1983 (**g**), 1983–2003 (**h**), and 2003–2010 (**i**). Negative values indicate mass loss. Uncertainties are reported as 1σ . Labels in **a** refer to Jakobshavn Isbræ (JI), Kangerlussuaq Glacier (KG), Zachariae Isstrøm (ZI), and Nioghalvfjærdsfjorden Glacier (NG), respectively. Labels in **c** refer to north (N), northeast (NE), central east (CE), central west (CW), northwest (NW), southwest (SW) and southeast (SE), respectively.

Table 1 | Mass balance and components LIA_{max}(1900)–2010

		GIS	SW	CW	NW	N	NE	CE	SE
LIA _{max} (1900)–1983	Mass balance	-75.1 ± 29.4	-8.7 ± 4.4	-7.9 ± 4.1	-27.6 ± 6.2	-2.9 ± 3.7	2.8 ± 4.1	-0.1 ± 2.3	-30.6 ± 4.5
	Revised SMB estimates ¹⁰	375.6 ± 84.5	39.9 ± 9.0	55.3 ± 12.4	65.6 ± 14.8	20.2 ± 4.5	8.5 ± 1.9	21.2 ± 4.8	164.9 ± 37.1
	Dynamic residual	-450.7 ± 89.5	-48.6 ± 10.0	-63.2 ± 13.1	-93.2 ± 16.0	-23.1 ± 5.9	-5.7 ± 4.5	-21.4 ± 5.3	-195.5 ± 37.4
1983–2003	Mass balance	-73.8 ± 40.5	-3.0 ± 2.9	-5.9 ± 3.4	-23.4 ± 6.4	-4.7 ± 6.8	0.7 ± 8.9	0.6 ± 6.5	-38.0 ± 5.5
	Revised SMB estimates ¹⁰	427.6 ± 96.2	50.1 ± 11.3	63.3 ± 14.2	69.2 ± 15.6	24.0 ± 5.4	9.3 ± 2.1	25.7 ± 5.8	186.0 ± 41.9
	Dynamic residual	-501.4 ± 104.4	-53.2 ± 11.6	-69.2 ± 14.6	-92.6 ± 16.8	-28.7 ± 8.7	-8.6 ± 9.2	-25.2 ± 8.7	-224.0 ± 42.2
2003–2010	Mass balance	-186.4 ± 18.9	-29.7 ± 4.6	-28.6 ± 3.0	-47.4 ± 2.1	-15.6 ± 1.3	-7.2 ± 2.0	-7.4 ± 2.2	-50.5 ± 3.6
	Revised SMB estimates ¹⁰	278.7 ± 62.7	6.9 ± 1.6	48.2 ± 10.9	50.9 ± 11.5	6.0 ± 1.4	5.1 ± 1.2	18.0 ± 4.0	143.5 ± 32.3
	Dynamic residual	-465.2 ± 65.5	-36.6 ± 4.9	-76.8 ± 11.3	-98.4 ± 11.7	-21.7 ± 1.9	-12.3 ± 2.4	-25.4 ± 4.6	-194.0 ± 32.5

Estimates of mass balance derived using the geodetic approach, the revised SMB estimates from ref. 10, and the dynamic residual of the GIS and the individual regions. Units, Gt yr⁻¹.

Figure 2a–c illustrates the annual mass balance for the three periods. We calculate a net mass loss of $6,233 \pm 2,436$ Gt (75.1 ± 29.4 Gt yr⁻¹) between the onset of glacial retreat from the LIA_{max} position (which we take to be 1900, as defined above) and 1983 (Fig. 2a). In northwest Greenland, where the majority of the ice sheet discharges through marine outlet glaciers, we find substantial and widely distributed thinning, leading to a mass loss of 27.6 ± 6.2 Gt yr⁻¹, corresponding to 37% of the total mass loss (Table 1). In west and southwest Greenland, we find peripheral thinning concentrated near the two large marine outlet glaciers Jakobshavn Isbræ and Kangiata Nunata Sermia. Substantial changes also occurred at the land-based glaciers Frederikshåb Isblink and Qassimiut Lobe, the latter being intersected by relatively small fjords draining its eastern part. Along the southeast coast, a region dominated by large marine outlet glaciers, thinning was extensive, in some areas propagating almost to the ice divide, causing a mass loss of 30.6 ± 4.5 Gt yr⁻¹ (41% of the total). Here two of the largest outlet glaciers in Greenland³, Kangerlussuaq Glacier and Helheim Glacier, show distinctly different patterns, with Kangerlussuaq Glacier being the single largest point source of mass loss (10.6 ± 1.2 Gt yr⁻¹), accounting for 14% of the total ice sheet mass loss during this period, while Helheim Glacier appears to have been near balance (mass gain equivalent to mass loss), despite the fact that front positions reveal a considerable inter-period variability^{9,14} of about 9 km. In east, northeast, and north Greenland thinning is less extensive and in some areas the ice margin remains at or very close to its LIA_{max} position, which in northern Greenland may be attributed to the confining effect of semi-permanent fjord ice on ice discharge¹⁵. The inference of persistent mass loss of the GIS since LIA_{max} may challenge the assumption of a near-balance ice sheet during the 1961–1990 period that is generally invoked to partition recent mass loss (that is, determine mass loss either by surface processes or ice discharge), and thus a failure to acknowledge mass loss during the reference period can result in overestimating the recent ice mass lost owing to surface mass balance (SMB) and ice dynamic processes¹⁶.

We calculate a total mass loss of $1,475 \pm 809$ Gt (73.8 ± 40.5 Gt yr⁻¹) for the period 1983–2003 (Fig. 2b). In general, peripheral ice thinning was less widespread and many of the largest outlet glaciers showed a decreasing mass loss (Table 1). During this period, 83% of the total mass loss occurred in the northwest and southeast while Jakobshavn Isbræ alone accounted for 6%, indicating that loss in the remainder of the ice sheet was limited. Interestingly, a comparison of our estimate with studies that have higher temporal resolution suggests that most of the overall, ice-sheet-wide mass loss that we record during 1983–2003 occurred in the late 1990s and early 2000s¹⁷ following a more stable period in the 1980s³.

Between 2003 and 2010, we estimate a mass loss of $1,305 \pm 132$ Gt (186.4 ± 18.9 Gt yr⁻¹), based on the ice mask we employed (Fig. 2c); when we used the same ice mask as ref. 18 (Methods, Extended

Data Fig. 3) we obtain a mass loss of 250.1 ± 21.2 Gt yr⁻¹, which is comparable to other studies^{2,17}. We find that 2003–2010 mass loss not only more than doubled relative to the 1983–2003 period, but also relative to the net mass loss rate throughout the twentieth century. This latter observation corroborates other studies which have inferred accelerated mass loss in the early twenty-first century relative to the late twentieth century^{3,5,19}. Many areas currently undergoing changes are identical to those which underwent considerable thinning throughout the twentieth century, with the exception of Helheim Glacier and the Nioghalvfjærdsfjorden Glacier (Fig. 2a–c). Consequently, comparing the twentieth-century thinning pattern to that of the last decade, and assuming a similar warming pattern, we suggest that the overall present mass loss pattern will persist for mass loss in the near future, at least until major marine outlet glaciers become land-terminating; though this may be biased because recent observations from northeast Greenland suggest a considerable acceleration in mass loss from Nioghalvfjærdsfjorden Glacier, following at least 20 years of dormancy, and from the Zachariae Isstrøm glacier¹⁸.

To assess the SMB and ice dynamic components of the twentieth-century mass balance we use updated SMB estimates from ref. 10 (Fig. 2d–f), which have been refined by implementing a more physically based meltwater retention scheme, and calibrating for better agreement with RACMO2.1/GR¹¹ during the period 1960–2012 (Methods). The ice dynamic residual is calculated by subtracting surface lowering caused by SMB processes from the reconstructed total mass balance (Fig. 2g–i) and is largely similar to the SMB pattern, though with positive values in the ablation zone and negative values in the accumulation zone. This general pattern is suggestive of an ice sheet close to balance; however, the residual also includes elevation trends due to forcing that is not included in the SMB model we employ. Perhaps unsurprisingly, we find a large dynamic contribution to the mass balance in the southeast and northwest, both dominated by marine-terminating glaciers, whereas in other regions the land-terminating ice sheet margin exhibits a positive dynamic mass contribution to compensate for the lowering of the ice surface due to SMB processes. Our results suggest that variability of the dynamic term of the GIS mass balance during the three intervals, which are LIA_{max}(1900)–1983, 1983–2003 and 2003–2010, is less than its associated uncertainties (Fig. 3a). Previous results have attributed the mass loss in 2000–2008 equally to decreasing SMB and to increasing discharge²⁰, while estimates for more recent periods suggest that decreasing SMB is becoming the dominant driver for increasing mass loss^{18,21}. Here we find that although short-term dynamic variability may affect the mass balance^{18,21–23}, on a centennial timescale the dominant driver for changes in the GIS mass balance so far appears to be variability in SMB (Fig. 3a).

The temporal variability of the mass balance during the twentieth century is computed as the difference between the updated SMB

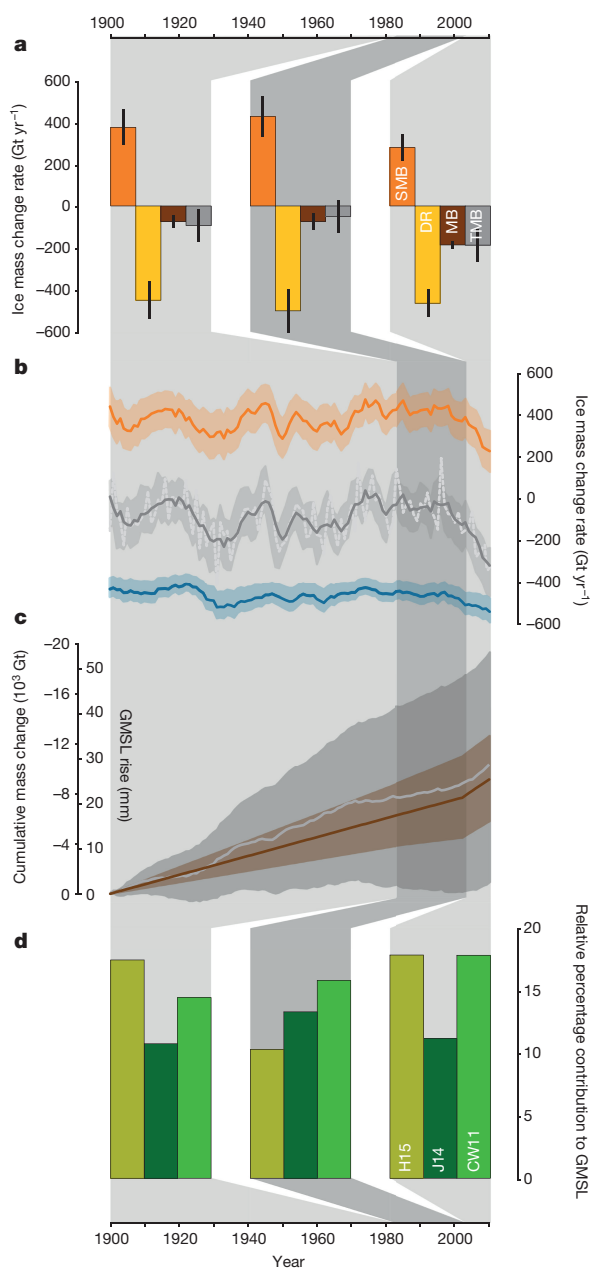


Figure 3 | Mass balance and implication of GMSL. **a**, Revised estimates of SMB from ref. 10 (orange bars), the ice dynamic residual (DR, yellow bars), mass balance based on the geodetic method (MB, dark brown bars), and mass balance based on the temporal mass balance approach (grey bars) covering the three periods LIA_{max}(1900)–1983, 1983–2003 and 2003–2010. Black lines represent the associated 1σ uncertainty ranges. The results suggest that variability in SMB affects long-term mass loss more strongly than does dynamic variability, which on a centennial timescale is more constant. **b**, The orange trace shows the 5-year running mean of the revised SMB estimates from ref. 10, the blue line represents the ice discharge modelled as a function of runoff using a 6-year trailing mean, and the dotted grey and solid grey lines show the yearly and 5-year running mean mass balance, respectively. The shaded areas reflect the associated 1σ uncertainty range (Methods). **c**, Cumulative mass change since LIA_{max}(1900) from the geodetic approach (brown line) and from the temporal mass balance reconstruction (grey line), and the shading gives the 1σ uncertainty ranges. **d**, The bars show the contribution of mass loss of the GIS relative to different solutions of the twentieth century GMSL rise from ref. 26 (H15, light green), ref. 27 (J14, dark green), and ref. 28 (CW11, green). Our result shows the minimum relative input of the GIS to sea level rise, which ranges between 10% and 18% during LIA_{max}(1900)–2010, supporting a substantial contribution from Greenland during the twentieth century.

estimates of ref. 10 and modelled ice discharge derived as a function of runoff^{5,24}, using a 6-year trailing mean, and ice discharge data from ref. 21 (Methods). During the period LIA_{max}(1900)–2010 we find a mass loss of $10,071 \pm 8,580$ Gt, which, despite the use of a smaller ice mask, is slightly higher than that of ref. 5. Although this ancillary temporal mass balance method is particularly sensitive to the ice discharge proxy employed, we find good absolute agreement with the mass loss of $9,013 \pm 3,378$ Gt found using the geodetic method presented above; this adds constraints and confidence to the results presented here.

Our temporal mass balance method suggests considerable variability in the mass balance during the twentieth century (Fig. 3b). The greatest negative mass balance rates occurred during the late 1920s and early 1930s, a period during which the rate of air temperature increase was higher than during the past decade^{14,25}, and which also coincides with extensive glacier retreat in southeast Greenland¹⁴. Following substantially lower or even nearly zero negative mass balance rates during the 1940s, our model results suggests mass loss rates during the 1950s and 1960s that are similar to those observed during the late 1990s and the early twenty-first century¹⁷. In the period covering the 1960s to the 1980s our results are comparable to other modelling results that generally suggest net mass loss during the 1960s and an ice sheet near balance during the 1970s to 1980s (ref. 3).

In the Fifth Assessment Report of the Intergovernmental Panel on Climate Change⁸, the twentieth-century global-mean sea level (GMSL) budget was assessed by comparing estimates derived from tide-gauges against observations of the different contributors, leading to unassigned residual sea level rise during 1901–1990. However, in ref. 8, no observational records of the contribution from GIS or the Antarctic Ice Sheet before 1993 are included. The failure to close the GMSL budget for the period 1901–1990 has been attributed to underestimation of the individual contributor factors, including the polar ice sheets^{1,8}. A recent study recalculated the twentieth-century GMSL using a probabilistic technique only to find a considerably lower rate of twentieth-century GMSL rise before 1993, thus closing the budget without including contributions from the polar ice sheets²⁶. However, our results show that during the twentieth century the GIS contributed substantially to GMSL rise (Fig. 3c).

In particular, the geodetic approach that is based on observations from aerial imagery, which indicates considerable thinning along the margin of the ice sheet, is regarded as a conservative minimum estimate of mass loss (Methods). We find using the geodetic approach a total mass loss of $9,013 \pm 3,378$ Gt from LIA_{max}(1900) to 2010, equivalent to 25.0 ± 9.4 mm of GMSL rise, and a mass loss of $10,071 \pm 8,580$ Gt (equivalent to 28.0 ± 23.8 mm GMSL rise) using our temporal mass balance method, and thus our results suggest that the GIS has contributed significantly to the twentieth-century sea level budget. Combining our geodetic-based results with recent GMSL reconstructions^{26–28} shows that in 1900–1983 the contribution from the GIS to GMSL rise ranged between 11% and 17%; in 1983–2003 it ranged between 10% and 16% and in 2003–2010 it ranged between 11% and 18% (Fig. 3d). Using the same ice mask as ref. 18 we find that during 2003–2010 the contribution to sea level rise ranged between 15% and 24%.

Thus far, any attempt to reconstruct long-term surface elevations beyond the scope of individual outlet glaciers has been prevented by the lack of a suitable Greenland-wide elevation model that would allow accurate observations of moraine and trimline heights representing the maximum ice sheet extent during the LIA. Our study provides 110 years of spatial and temporal mass balance of the GIS and in addition centennial estimates of the SMB and dynamic terms of the mass balance. Finally, our conservative, observation-based results, showing considerable mass loss during the twentieth century from the GIS, minimize the unassigned residual GMSL rise during 1901–1990. This will help to close the twentieth-century GMSL budget, which is crucial for evaluating the reliability of modelling contributions to past sea level rise, and hence for increasing confidence in projections of sea level rise^{1,8}.

Online Content Methods, along with any additional Extended Data display items and Source Data, are available in the online version of the paper; references unique to these sections appear only in the online paper.

Received 4 May; accepted 26 October 2015.

- Gregory, J. M. *et al.* Twentieth-century global-mean sea level rise: is the whole greater than the sum of the parts? *J. Clim.* **26**, 4476–4499 (2013).
- Khan, S. A. *et al.* Greenland ice sheet mass balance: a review. *Prog. Phys.* **78**, 046801 (2015).
- Rignot, E., Box, J. E., Burgess, E. & Hanna, E. Mass balance of the Greenland ice sheet from 1958 to 2007. *Geophys. Res. Lett.* **35**, L20502 (2008).
- Yanga, L. A southern Greenland ice sheet glacier discharge reconstruction: 1958–2007. *Phys. Procedia* **22**, 292–298 (2011).
- Box, J. E. & Colgan, W. Greenland ice sheet mass balance reconstruction. Part III: marine ice loss and total mass balance (1840–2010). *J. Clim.* **26**, 6990–7002 (2013).
- van de Wal, R. & Oerlemans, J. An energy balance model for the Greenland ice sheet. *Global Planet. Change* **9**, 115–131 (1994).
- Zuo, Z. & Oerlemans, J. Contribution of glacier melt to sea-level rise since AD 1865: a regionally differentiated calculation. *Clim. Dyn.* **13**, 835–845 (1997).
- Church, J. A. *et al.* in *Climate Change 2013: The Physical Science Basis. Contribution of Working Group I to the Fifth Assessment Report of the Intergovernmental Panel on Climate Change* (eds Stocker, T. F. *et al.*) 1137–1216 (Cambridge Univ. Press, 2013).
- Khan, S. A. *et al.* Glacier dynamics at Helheim and Kangerdlugssuaq glaciers, southeast Greenland, since the Little Ice Age. *Cryosphere* **8**, 1497–1507 (2014).
- Box, J. E. Greenland ice sheet mass balance reconstruction. Part II: surface mass balance (1840–2010)*. *J. Clim.* **26**, 6974–6989 (2013).
- van Angelen, J. H., van den Broeke, M. R. & van de Berg, W. J. Momentum budget of the atmospheric boundary layer over the Greenland ice sheet and its surrounding seas. *J. Geophys. Res.* **116**, D10101 (2011).
- Csatho, B. M., Schenk, T., van der Veen, C. J. & Krabill, W. B. Intermittent thinning of Jakobshavn Isbræ, West Greenland, since the Little Ice Age. *J. Glaciol.* **54**, 131–144 (2008).
- Lea, J. M. *et al.* Terminus-driven retreat of a major southwest Greenland tidewater glacier during the early 19th century: Insights from glacier reconstructions and numerical modelling. *J. Glaciol.* **60**, 333–344 (2014).
- Bjørk, A. A. *et al.* An aerial view of 80 years of climate-related glacier fluctuations in southeast Greenland. *Nat. Geosci.* **5**, 427–432 (2012).
- Higgins, A. K. North Greenland glacier velocities and calf ice production. *Polarforschung* **60**, 1–23 (1990).
- Colgan, W. *et al.* Greenland high-elevation mass balance: inference and implication of reference period (1961–90) imbalance. *Ann. Glaciol.* **56**, 105–117 (2015).
- Shepherd, A. *et al.* A reconciled estimate of ice sheet mass balance. *Science* **338**, 1183–1189 (2012).
- Khan, S. A. *et al.* Sustained mass loss of the northeast Greenland ice sheet triggered by regional warming. *Nature Clim. Change* **4**, 292–299 (2014).
- Rignot, E., Velicogna, I., van den Broeke, M. R., Monaghan, A. & Lenaerts, J. T. M. Acceleration of the contribution of the Greenland and Antarctic ice sheets to sea level rise. *Geophys. Res. Lett.* **38**, L05503 (2011).
- van den Broeke, M. *et al.* Partitioning recent Greenland mass loss. *Science* **326**, 984–986 (2009).
- Enderlin, E. M. *et al.* An improved mass budget for the Greenland ice sheet. *Geophys. Res. Lett.* **41**, 866–872 (2014).
- Kjær, K. H. *et al.* Aerial photographs reveal late-20th-century dynamic ice loss in northwestern Greenland. *Science* **337**, 569–573 (2012).
- Howat, I. M., Joughin, I. R. & Scambos, T. A. Rapid changes in ice discharge from Greenland outlet glaciers. *Science* **315**, 1559–1561 (2007).
- Bamber, J., van den Broeke, M. R., Ettema, J., Lenaerts, J. & Rignot, E. Recent large increases in freshwater fluxes from Greenland into the North Atlantic. *Geophys. Res. Lett.* **39**, L19501 (2012).
- Box, J. E., Yang, L., Bromwich, D. H. & Bai, L.-S. Greenland Ice Sheet surface air temperature variability: 1840–2007*. *J. Clim.* **22**, 4029–4049 (2009).
- Hay, C. C., Morrow, E., Kopp, R. E. & Mitrovica, J. X. Probabilistic reanalysis of twentieth-century sea-level rise. *Nature* **517**, 481–484 (2015).
- Jevrejeva, S., Moore, J. C., Grinsted, A., Matthews, P. & Spada, G. Trends and acceleration in global and regional sea levels since 1807. *Global Planet. Change* **113**, 11–22 (2014).
- Church, J. A. & White, N. J. Sea-level rise from the late 19th to the early 21st century. *Surv. Geophys.* **32**, 585–602 (2011).
- Kobashi, T. *et al.* On the origin of multidecadal to centennial Greenland temperature anomalies over the past 800 yr. *Clim. Past* **9**, 583–596 (2013).
- Weidick, A., Bennike, O., Citterio, M. & Nørgaard-Pedersen, N. Neoglacial and historical glacier changes around Kangarsuneq fjord in southern West Greenland. *Geol. Surv. Denmark Greenland Bull.* **27**, 1–68, <http://www.geus.dk/publications/bull/nr27/index-uk.htm> (2012).

Acknowledgements This study would not have been possible without the aid of The Danish Geodata Agency (GST), who gave us access to their historical aerial photographs. This work is a part of the X_Centuries project funded by the Danish Council for Independent Research (FNU) (grant number DFF-0602-02526B) and the Centre for GeoGenetics supported by the Danish National Research Foundation (DNRF94). K.K.K. acknowledges support from the Danish Council for Independent Research (FNU) and the Sapere Aude: DFF-Research Talent programme (grant number DFF-4090-00151). J.E.B., K.H.K. and N.K.L. acknowledge support by the GeoCenter Denmark (“Multi-millennial ice volume changes of the Greenland ice sheet”). S.A.K. acknowledges supports from the Carlsberg Foundation (grant number CF14-0145) and the Danish Council for Independent Research (FNU) (grant number DFF-4181-00126). M.v.d.B. acknowledges support from the Netherlands Polar Program of the Netherlands Organization of Scientific Research (NWO). C.N. acknowledges support by the European Research Council (EUP7/ERC grant number 320816). We thank A. J. Long, S. A. Woodroffe, B. M. Vinther, and R. Hurlmans for contribution during the early phase of this study.

Author Contributions K.K.K. and K.H.K. designed and conducted the study. N.J.K. did photogrammetric modelling and aero-photogrammetric DEM processing, and quality control and validation with C.N. K.K.K. undertook the Geographical Information System analysis. A.A.B. conducted the manual photogrammetry measurements. S.A.K. carried out analysis of surface elevation data, developed the scaling method, and made the mass balance calculations. J.E.B., J.L.B., and M.v.d.B. provided SMB model and context. W.C., J.E.B., and K.K.K. performed temporal discharge and mass balance modelling. S.F. and N.K.L. provided the historical context of ice sheet extent. All authors contributed to discussion and writing of the manuscript.

Author Information Reprints and permissions information is available at www.nature.com/reprints. The authors declare no competing financial interests. Readers are welcome to comment on the online version of the paper. Correspondence and requests for materials should be addressed to K.H.K. (kurtk@snm.ku.dk).

METHODS

Elevation changes between LIA_{max} and 1978–87 are derived from direct observations of LIA_{max} moraines and trimlines and the ice surface in vertical stereo photogrammetric imagery recorded during 1978–87. Changes are extrapolated to the ice sheet interior using a scale-value approach based on aerial and satellite altimeter data from the period 2003–2010, with site-specific interpolations in 82 basins around the ice sheet. The same scaling approach is used to derive changes from 1978–87 to 2003. For the entire LIA_{max} –2010 period we use annual estimates from a SMB model¹⁰ to quantify mass balance processes and to assess temporal variability of the mass balance components through time. In-depth descriptions of the methods used are provided below.

Geometric approach to derive surface elevation changes. Previously, mass balance estimates of the entire GIS have been based on modelling efforts that rely on empirical relations between SMB and ice discharge^{3–5} or energy balance modelling^{6,7}. Geometric approaches have been applied to Jakobshavn Isbræ¹², outlet glaciers in Patagonia³¹, and land-terminating glaciers on James Ross Island, Antarctic³², by mapping trimlines and lateral and end moraines. These studies, however, focus on single-outlet glaciers from the GIS, smaller ice caps, or small isolated glaciers, respectively. Each study used varying methods to account for elevation changes at higher elevations inland, for example, finding upper boundary changes by vertical shifting of the contemporary equilibrium line altitude based on lapse rate temperature reconstructions³¹, or by the vertical difference between trimlines and ice surfaces to provide elevation offsets and thereby estimate mass loss³².

Here, we outline the geometric method we deployed that allows us to translate point observations of former ice margin position to an ice-sheet-wide mass balance. The height of an equilibrium glacier or ice sheet profile can be expressed as (see, for example, ref. 33):

$$h(x) = H \left(1 - \left(\frac{x}{L} \right)^{1+1/n} \right)^{1/(2+2/n)} \quad (1)$$

where H is the surface elevation at the ice divide, L is the length of the ice sheet profile, h is the surface elevation at distance x from the ice divide, and the exponent n is a constant. This relation assumes no sliding, a flat bed, uniform accumulation, and constant flowband width. Here, we apply it to show that by using elevation changes between time t_1 and time t_2 it is possible to estimate elevation changes during another period, for example, time t_1 and time t_3 , or to extend the estimate further, for example between time t_3 and time t_4 , by scaling elevation changes of the known period. Subsequently, the approach is assessed using observations at three main outlet glaciers in Greenland: Kangerlussuaq Glacier, Helheim Glacier, and Jakobshavn Isbræ.

However, first we consider three ice surface profiles h , from the ice divide to the ice margin, using typical values for the GIS. Each surface elevation profile represents one of the time steps t_1 , t_2 and t_3 . The glacier length from the ice divide L is in this example $x = 200,000$ m at t_1 , and changes by 1,000 m for each time step, while the ice divide height H is kept constant at 3,300 m, and the exponent n is set to 3 (Extended Data Fig. 1a). We simulate surface changes by changing the glacier length L (this corresponds to advance or retreat of the ice margin), and thus surface elevation changes at x are governed by the total length of the ice profile. In our example, the ice retreats from the initial time step t_1 by 1,000 m and the ice surface lowers at t_2 . Next, we predict the ice profile at t_3 by applying a scale-value and define the predicted profile 3 (h_{pre_t3}) (Extended Data Fig. 1b) as:

$$h_{pre_t3} = h_{t1} + S(h_{t2} - h_{t1}) \quad (2)$$

where S is a constant.

Comparing the elevation changes between h_{t1} and h_{t3} (dh_{t1t3}) and those between h_{t1} and h_{pre_t3} (dh_{t1t3_pre}), derived using equation (2) and an S -value of 2.2, shows overall agreement, though also differences near the margin (Extended Data Fig. 1c). However, here the surface profile h_{t1} is part of both the input and of the output. To generate a predicted difference where the same timestamp (for example, t_1) is not incorporated in the input and the output, the S can be altered and an 'independent' dh estimate may be calculated. Here, $h_{t2} - h_{t1}$ (dh_{t1t2}) and an S -value of 1.2 simulates dh_{t3t4_pre} , which shows overall agreement with $h_{t3} - h_{t4}$ (dh_{t3t4}), but again also differences near the margin (Extended Data Fig. 1d). Nevertheless, it implies that if dh_{t1t2} and dh_{t3t4} are both known the constant S can be derived as the ratio between these values.

Extended Data Fig. 1e shows the difference between profile h_{t3} and h_{pre_t3} using a constant S . Over large parts of the profile the difference is small (< 1 m), however, near the margin differences increase to tens of metres. We use the difference as an expression of the constant S and denote it σ_{Smeth} (and include it in our

mass balance uncertainty calculations). Extended Data Fig. 1f shows change in elevation (in metres) between two timestamps as a function of surface elevation. Thinning is largest at lower elevations, but drops rapidly and become close to 0 at $h > 2,500$ m.

We note that, considering the differences near the margin (Extended Data Fig. 1e), the profile approach employed does not work (well) near the terminus of marine-terminating outlet glaciers. As discussed in Methods section 'Uncertainties and conservative mass balance estimates', however, we use an ice mask derived from aerial images recorded during 1978–87, and thus the large differences between simulated and predicted surface profiles, that is, σ_{Smeth} (Extended Data Fig. 1e) and large elevation changes (Extended Data Fig. 1f) at low elevations are not included in the estimate of the period between LIA_{max} (1900) to 1978–87.

The approach presented here is founded in the relation in equation (1), for which certain assumptions are made. These assumptions are violated for a large part of the ice sheet. For instance, basal sliding is considerable near marine-terminating outlet glaciers, which combined drain 88% of the ice sheet, and over the majority of the entire ice sheet basal-sliding motion dominates over internal deformation³⁴. Extended Data Fig. 2 provides three examples where we apply our approach to major marine-terminating outlet glaciers. Here, we compare elevation changes derived using our scaling approach with elevation changes derived from the DEM (see Methods section 'Photogrammetric DEM 1978–87') and 2003 NASA Airborne Topographic Mapper (ATM) flight lines³⁵. We find good agreement (within uncertainties) between the observed and predicted elevation change rates. The examples in Extended Data Fig. 2 illustrate the validity of our approach in fast-flowing areas, where basal sliding is considerable, the bed is not flat, the accumulation is non-uniform, and the width of the flowband is not constant, that is, where the assumptions of the relation in equation (1) are violated. Moreover, the combined uncertainty that we estimate includes an uncertainty related to the scaling approach (σ_{Smeth}), an error related to changes during 2003–2010 (dh_{solid}) (see Methods section '2003–2010 elevation changes from air- and space-borne laser altimetry'), and an uncertainty related to the scaling of point-based observations, for example, dh_{LIA} (see Methods section 'LIA_{max} to 1978–87 mass balance'), and thereby the combined uncertainty estimate accounts for the scaling of the observations, and thereby incorporates the variability between observations and dh_{solid} . Thus, we regard the comparison illustrated in Extended Data Fig. 2 as a validation of our approach to derive ice-sheet-wide mass balance estimates.

2003–2010 elevation changes from air- and space-borne laser altimetry. To detect ice surface elevation changes from April 2003 to April 2010, which serves as the base data set from which to calculate a scale value, we use all available Ice, Cloud, and land Elevation Satellite (ICESat) GLA12 Release 31 data³⁶. ICESat elevations have a crossover standard deviation of $\sigma_{ICESat} = 0.2$ m (refs 37–39). Furthermore, we use all available NASA ATM flight lines³⁵ between 2003 and 2010, and NASA's Land, Vegetation, and Ice Sensor (LVIS) flight lines from 2010 (ref. 40), both of which have an uncertainty of 0.1 m. Ice surface elevation changes and associated uncertainties during the period April 2003 to April 2010 are derived in $1 \text{ km} \times 1 \text{ km}$ cells and converted into an ice sheet surface elevation change grid ($dh_{2003-2010}$)^{18,38,41–43}.

Using SMB fields from RACMO2.1/GR output¹¹ the elevation change due to firm compaction is calculated^{18,42} and subtracted from the total elevation change ($dh_{2003-2010}$), thereby yielding an elevation change due to solid ice changes (dh_{solid}) on a $1 \text{ km} \times 1 \text{ km}$ grid.

As part of our calculation, we divide the ice sheet into drainage basins (Extended Data Fig. 3). Here, we use the drainage basins from ref. 44 divided into sub-basins and we include additional areas around the ice sheet margin, yielding a total of 82 basins. Some areas on the southeast coast were omitted due to the lack of LIA input data, mainly caused by extensive snow cover at the time of acquisition of the aerial stereophotographs. Additionally, we use the Randolph Glacier Inventory, version 3.2 (ref. 45) to exclude glaciers not connected to the ice sheet and those only weakly connected, RGIFlag CL0 and CL1, respectively.

Measuring LIA elevations from aerial photographs. To detect ice surface elevation changes from LIA_{max} to 1978–87 we use aero-triangulated vertical stereo photogrammetric imagery recorded during 1978–1987. The images were recorded between late July and mid-August from an altitude of 13,500 m to a scale of 1:150,000. They are part of a larger collection of images covering the entire ice-free part of Greenland, processed at the Anthropocene and Quaternary Research Group of the Centre for GeoGenetics, Natural History Museum of Denmark.

The aerial photographs were processed in the SOCET SET 5.6. software package written by BAE Systems using GR96 aero-analytical triangulated control points surveyed with GPS and provided by The Danish Geodata Agency⁴⁶, a part of the Danish Ministry of Energy, Utilities and Climate. The processed aerial photographs allow us to survey trimlines, ice margins and moraines outlining

the LIA_{max} in three dimensions with high accuracy. In the survey two types of points have been defined and measured: type 1, trimline or lateral moraines; and type 2, an active front.

Each of these types contains two surveyed data points: LIA_{max} and the 1978–87 position and elevation of the ice margin (Extended Data Fig. 4). For type 1 the LIA_{max} extent is determined from the trimline between the non-eroded and the freshly ice scoured bedrock or lateral moraines⁹. Type 2 determines the position of end moraines or other geomorphic evidence of recent glacially overridden landscape.

The data type distribution is illustrated in Extended Data Fig. 5a while Extended Data Fig. 5b illustrates the elevation difference at 3,003 points between LIA_{max} and 1978–87 derived from 6,006 manual point measurements.

The elevation differences derived from the three-dimensional stereo-photogrammetric single-point survey (dh_{LIA} values) are assigned an uncertainty of 1 m as almost all systematic error affecting the triangulation of the images is eliminated⁹. Moreover, since the LIA_{max} extent is mapped on the 1978–87 images we can ignore post-depositional effects on the moraines and glacial isostatic adjustment correction⁹.

LIA_{max} to 1978–87 mass balance. The ice mass balance since the LIA_{max} is calculated by scaling dh_{LIA} values to the elevation changes between 2003 and 2010 (dh_{solid}). We use the dh_{LIA} points at outlet glaciers of variable sizes (land- and marine-terminating) as well as other areas of the ice margin to determine the scale value (S_{LIA}), derived as the ratio between the point-based dh_{LIA} and dh_{solid} of the closest grid cell. This implies that the shape of the ice profiles for different timestamps is not (directly) used; rather, we use dh point values that show the point-based thinning pattern along the periphery to derive the ice-sheet-wide thinning pattern. Subsequently, the S_{LIA} values found for each glacier are interpolated using the weighted mean to a regular 1 km × 1 km grid for each of the 82 calculation basins (Extended Data Fig. 3). For each grid point we predict an S value and assign an uncertainty, $\sigma_{S(LIA_rms)}$, based on the root mean square of the predicted values within the basin. However, the total uncertainty $\sigma_{S(LIA)}$ of S values has to account for the $\sigma_{S(meth)}$ (see Methods section ‘Geometric approach to derive surface elevation changes’). Thus for each grid point i we obtain:

$$\sigma_{S(LIA)}^i = \sqrt{(\sigma_{S(LIA_rms)}^i)^2 + (\sigma_{S(meth)}^i)^2} \quad (3)$$

Next, the elevation change between LIA_{max} and 1978–87 are calculated by multiplying the S_{LIA} grid and the elevation change due to solid ice changes (dh_{solid}) between 2003 and 2010:

$$dh_{LIA}^i = S_{LIA}^i dh_{solid}^i \quad (4)$$

where i represents each cell on a regular 1 km × 1 km grid. By using dh_{solid} , which includes changes in elevation due to firn compaction, we thereby obtain estimates of the mass balance.

To each value of dh_{LIA} we assign uncertainty as follows:

$$\sigma_{dh_{LIA}}^i = dh_{LIA}^i \sqrt{\left(\frac{\sigma_{S(LIA)}^i}{S(LIA)^i}\right)^2 + \left(\frac{\sigma_{dh_{solid}}^i}{dh_{solid}^i}\right)^2} \quad (5)$$

The calculation allows us to ignore the actual timing of the maximum extent during LIA because it is mapped on the 1978–87 images, thereby making it directly applicable to derive ice net mass balance between LIA_{max} and 1978–87. However, to obtain a rate we assign 1900 as a Greenland-wide time stamp of when the glaciers started to retreat following the LIA, although we note that there is regional and local variability^{9,12,13}, and use 1983 as the average year of the aerial imagery. **Photogrammetric DEM 1978–87.** We produced a 25 m × 25 m digital elevation model (DEM1978/87) using the vertical stereo photogrammetric imagery recorded during 1978–1987 following a standard approach^{18,22}. The DEM is processed into WGS84 ellipsoid heights, directly comparable to ICESat, ATM, and LVIS data.

Our validation methodology is based upon co-registration methods that relate the three-dimensional co-registration vector between two elevation surfaces to terrain slope α and aspect ψ (refs 47 and 48). The co-registration parameters are determined by robust least-squares minimizations of stable terrain elevation changes between the DEM tiles and ICESat³⁶ (dh) using:

$$dh = a \cos(b - \psi) \tan(\alpha) + c \quad (6)$$

where a and b is the magnitude and direction, respectively, of the horizontal co-registration vector and c is the mean vertical bias between the two elevation data sources.

We perform the co-registration on a 50 km × 50 km grid over all the DEM. All slopes less than 5° are removed and a curvature filter is applied to remove regions where resolution variation between the data sets may cause spurious elevation differences.

The co-registration parameters are generally less than 15 m horizontally and less than 10 m vertically. At the 1 σ confidence level, the aero-photogrammetric DEM has an accuracy of 10 m horizontally and 6 m vertically while the precision is better than 4 m (Extended Data Fig. 6). We note that the 6 m vertical accuracy of the DEM is different from the 1 m uncertainty related to dh_{LIA} values obtained in the three-dimensional stereo-photogrammetric single-point survey (see Methods section ‘LIA_{max} to 1978–87 mass balance’).

1978–87 to 2003 mass balance. The mass balance between 1978–87 and 2003 is determined using the same approach as outlined for calculating the LIA_{max} to 1978–87 mass balance but with different input data. We use ATM data from 2010 (ref. 35), supplemented with 2009 ICESat data³⁶ to fill in gaps, to determine the mass balance between 1978–87 and 2010. Subsequently, we subtract the derived mass balance between 2003 and 2010 to determine the 1978–87 to 2003 mass balance.

The merged ATM and ICESat data cover outlet glaciers of variable size and termination regime. At these data points, elevations from the 1978–87 DEMs are extracted, although we remove interpolated DEM surfaces using a reliability mask¹⁸, an output produced during DEM production. The point-based difference between the ATM/ICESat measured surface elevation and the DEM elevation is dh_{80s-10} . To accommodate issues related to large differences between simulated and predicted surface profiles (see Methods section ‘Geometric approach to derive surface elevation changes’) we use point observations only up-glacier from the terminus, though the distance varies for individual outlet glaciers with the location of available ATM and ICESat data.

Next, we derive the S_{80s-10} value as the ratio between the point-based dh_{80s-10} and a dh_{solid} value extracted from the 1 km × 1 km grid using bilinear interpolation between grid cells. The S_{80s-10} values are subsequently interpolated using a weighted mean to a regular 1 km × 1 km grid. Thus for each grid point we predict a S value and assign an uncertainty, $\sigma_{S(80s-10_rms)}$, based on the root mean square of the predicted values within the basin. However, the total uncertainty $\sigma_{S_{80s-10}}$ of S values has to account for the $\sigma_{S(meth)}$ (see Methods section ‘Geometric approach to derive surface elevation changes’). Thus, for each grid point i we obtain:

$$\sigma_{S(80s-10)}^i = \sqrt{(\sigma_{S(80s-10_rms)}^i)^2 + (\sigma_{S(meth)}^i)^2} \quad (7)$$

The elevation change between 1978–87 and 2010 is calculated by multiplying the S_{80s-10} grid and the dh_{solid} (2003–2010) grid:

$$dh_{80s-10}^i = S_{80s-10}^i dh_{solid}^i \quad (8)$$

where i represents each cell on a regular 1 km × 1 km grid.

To each value of dh_{80s-10} we assign an uncertainty of:

$$\sigma_{dh_{80s-10}}^i = dh_{80s-10}^i \sqrt{\left(\frac{\sigma_{S(80s-10)}^i}{S_{80s-10}^i}\right)^2 + \left(\frac{\sigma_{dh_{solid}}^i}{dh_{solid}^i}\right)^2} \quad (9)$$

Subsequently, we subtract dh_{solid}^i from dh_{80s-10}^i to determine the mass balance from 1978–87 to 2003.

Uncertainties and conservative mass balance estimates. For the entire ice sheet (or individual basins) we calculate the uncertainty of the mass balance estimates during LIA_{max} to 1978–87 and 1978–87 to 2003 as:

$$\sigma_{POI} = \sum_{i=1}^n \sigma_{dh_{POI}}^i \quad (10)$$

where $\sigma_{dh_{POI}}^i$ is the uncertainty of each grid point during the period of interest (LIA_{max} to 1978–87 or 1978–87 to 2003) derived from equation (5) or equation (9) and n is the number of points covering the basin, region, or entire ice sheet being considered.

We regard the derived mass balance estimates between LIA_{max} and 1978–87 as conservative for a number of reasons. First, when calculating mass balance we are limited by the spatial extent of our ice mask, which implies that mass loss between the boundary of the ice mask (based on the ice extent derived from the 1978–87 aerial images) and the maximum extent of the glaciers during the LIA is not included. This zone of non-included ice loss is largest near marine-terminating glaciers. For example Jakobshavn Isbræ retreated by about 20 km between LIA_{max} and 1978–87, while Kangerlussuaq Glacier and Midgaard Glacier retreated by about 12 km and about 20 km, respectively, during the same period. Here, the outer parts of the glaciers may have been afloat during the LIA and would already then

have contributed to GMSL rise, while only mass loss up-glacier from the LIA_{max} grounding line would contribute to post-LIA sea level rise. As the extent of the ice mask is not identical to the LIA_{max} grounding line we cannot capture the mass loss between these two.

Second, owing to the lack of LIA data on the southeast some areas are excluded, and so are glaciers not connected to the ice sheet and those only weakly connected, RGIFlag CL0 and CL1, respectively⁴⁵. This may lead to a smaller mass balance estimate for the different periods; for example we estimate a mass loss of $186.4 \pm 18.9 \text{ Gt yr}^{-1}$ for the period 2003–2010, while using the same ice mask as ref. 18 we arrive at a mass loss of $250.1 \pm 21.2 \text{ Gt yr}^{-1}$.

Third, propagation of thinning at the ice margin towards the interior is not incorporated in the present model, as we use a scaling approach based on point-based thinning observations at the periphery of the ice sheet to estimate the mass balance. Model experiments suggest that mass loss at lower elevations would propagate inland and cause interior thinning on decadal timescales and continue inland even if mass loss at the ice margin ceases⁴⁹. For all three periods we calculate a mass gain in the interior of the ice sheet, which since 1993 has also been identified by others^{50–52}. Verifying mass gain in the interior for the period LIA_{max} to 1978–87 (1983) is difficult because ice-core-derived estimates of ice surface elevation changes are associated with vertical uncertainties of about 70 m (ref. 53). Excluding the interior mass gain during LIA_{max} –1983 yields a mass loss of $7,712 \pm 1323 \text{ Gt}$ ($92.9 \pm 15.9 \text{ Gt yr}^{-1}$) relative to the conservative estimate of $6,233 \pm 2436 \text{ Gt}$ ($75.1 \pm 29.4 \text{ Gt yr}^{-1}$).

Even though the individual contribution of the abovementioned assumptions to mass loss may be considered minor, the combined effects may be considerable. However, given the limitations in the present model configuration and lack of observations to constrain the behaviour of the interior mass balance, we favour the conservative estimate presented in this paper and emphasize that it should be regarded as a minimum contribution from the GIS to GMSL rise during the period LIA_{max} to 1978–87 (1983).

SMB modelling. The near-surface air temperature T and the land-ice SMB (that is, total precipitation minus total sublimation minus runoff) reconstruction of ref. 10, spanning 1840–2012, is calibrated to RACMO2.1/GR output¹¹. The calibration is important because SMB fields from RACMO2.1/GR are used as input to convert total elevation during 2003–2010 ($dh_{2003-2010}$) into elevation change due to solid-ice changes (dh_{solid}) using a firn-compaction model (see Methods section ‘2003–2010 elevation changes from air- and space-borne laser altimetry’). Thus, because we use dh_{solid} to calculate mass balance estimates during LIA_{max} –1983 and 1983–2003, it is critical that the two SMB models are comparable when assessing the components of the twentieth-century mass balance. Furthermore, owing to sharply decreasing ice core data availability after 1999, from which snow accumulation is derived in the SMB model of ref. 10, the model incorporates precipitation fields from RACMO2.1/GR. The calibration of T and the SMB components excluding snow accumulation employs a 53-year overlap period (1960–2012), whereas snow accumulation is calibrated during the 1960–1999 period. The calibration employs linear regression coefficients at each 5-km grid cell that match the multi-year average of the reconstruction with that from RACMO2.1/GR. Prior to calibration the RACMO2.1/GR data are resampled/reprojected from their native 0.1° ($\sim 11 \text{ km}$) grid to the 5-km grid employed by ref. 10. A 5%–8% correction is applied in SMB totals to account for the 5-km polar stereographic grid cell area variation with latitude.

Refinements are applied to the original SMB reconstruction¹⁰ as follows. (1) Values are now estimated over all land, sea, and ice within the domain, rather than over only ice. (2) A physically based meltwater retention scheme⁵⁴ replaces the original simpler approach. (3) Multiple stations now contribute to the T value for each given month and grid cell within the domain, rather than employing the single highest-correlating station. (4) The RACMO2.1/GR data used for calibration have a higher native resolution ($\sim 11 \text{ km}$) than the Polar MM5 data ($\sim 24 \text{ km}$) used to calibrate the original SMB reconstruction. (5) The SMB reconstruction now extends to 2012, rather than 2010. (6) The ice-core-derived annual accumulation rates are divided into monthly temporal resolution by weighting the monthly fraction of annual accumulation after the 1960–2012 average RACMO2.1/GR seasonal distribution at each grid cell.

Absolute uncertainty for the revised SMB estimates from ref. 10 is estimated by comparing against field data. *In situ* annual ablation rates ($n = 208$), spanning 1985–1992, yield an ablation root-mean-square error of 35%. This is analogous to an *in situ* comparison with RACMO2.1/GR. Comparison between revised SMB estimates from ref. 10 (or RACMO2.1/GR) with ice-core-derived net accumulation time series from 86 sites⁵⁵ yields a 30% accumulation root-mean-square error.

A fundamental assumption is that the calibration regression factors (slope and intercept), derived on a grid cell basis during 1960–2012 versus ice cores, meteorological station temperatures, and with RACMO2.1/GR, are stationary in time. Testing this, we find that over the 53-year overlap period (1960–2012) cumulative

SMB anomalies drift between the reconstruction and RACMO2.1/GR by up to 600 Gt as compared to a total mass flux of 24,000 Gt, suggesting a drift uncertainty of 2.5%. In the pre-1960 period, cumulative uncertainty may be larger.

Temporal variability of the mass balance. To assess the variability of the mass balance during the twentieth century we use an approach similar to that of other studies^{3,5,24}. Here iceberg discharge is estimated using a linear regression between reconstructed meltwater runoff from revised SMB estimates from ref. 10 and estimates of ice-sheet-wide iceberg discharge, spanning 2000–2012 (ref. 21). We find a peak correlation ($r = 0.87$; $P < 0.01$; degrees of freedom = 12) between annual iceberg discharge D and six-year mean meltwater runoff R_6 , calculated from the five years preceding, and including a given year. D_M is modelled ice discharge in gigatonnes per year and is calculated as follows:

$$D_M = 0.766R_6 + 266 \quad (11)$$

This is similar to employing a correlation between five-year lagging meltwater runoff and annual iceberg discharge²⁴. We use the discharge estimates of ref. 21, though we note that the estimates generally lie within uncertainties of other studies^{3,5,6} except those of ref. 24 (Extended Data Fig. 7). Uncertainties related to the temporal mass balance method are calculated using Monte Carlo simulation (see Methods section ‘Estimating uncertainties using Monte Carlo simulation’).

Estimating uncertainties using Monte Carlo simulation. We implement a Monte Carlo uncertainty approach that accounts for the interaction of uncertainties in mass balance components⁵. The residual root-mean-square differences between revised SMB estimates from ref. 10 and RACMO2.1/GR are increased by 50% to form a conservative uncertainty estimates given that the absolute uncertainty may be larger than the calibration root-mean-square difference. The post-calibration root-mean-square difference for runoff is increased by 50% yielding an assumed conservative uncertainty of 24.9%. That for accumulation is 8.0% and that for SMB is 22.5%. These are relative uncertainties between RACMO2.1/GR and revised SMB estimates from ref. 10. Absolute uncertainty is evaluated relative to field data.

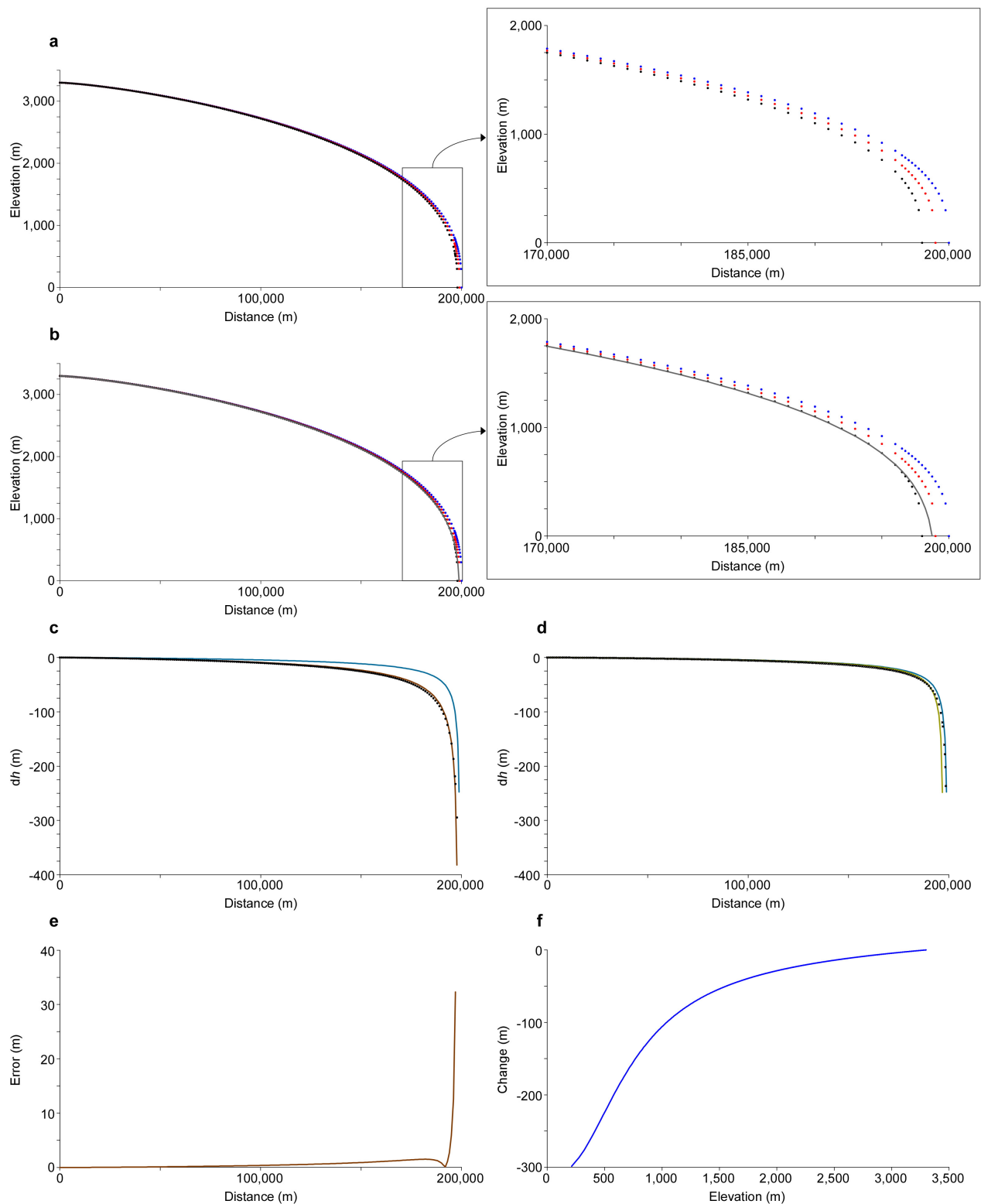
Because iceberg discharge is a function of runoff, the runoff uncertainty is propagated through Eq. (11) to estimate iceberg discharge uncertainty. The temporal mass balance uncertainty is estimated as 78 Gt yr^{-1} . Extended Data Fig. 8 shows the Monte Carlo simulation for the temporal mass balance expressed as cumulative eustatic sea level change during 1840–2012.

Data. We use aero-triangulated vertical stereo photogrammetric imagery recorded during 1978–1987 to manually map the former ice extent during the LIA_{max} . Raw imagery was made available for research purposes by The Danish Geodata Agency, a part of the Danish Ministry of Energy, Utilities and Climate. The derived products used in this study such as orthophotos and the DEM are available in GeoTiff format upon request to the corresponding author. Moreover, we use all available ICESat GLA12 Release 31 data³⁶ (<https://nsidc.org/data/icesat/data.html>) and all available NASA ATM flight lines³⁵ between 2003 and 2010 (<http://nsidc.org/data/blatm2> and <https://nsidc.org/data/ilatm2>) and NASA’s LVIS flight lines⁴⁰ from 2010 (<https://nsidc.org/data/ilvis2>). Information on SMB data from RACMO2.1/GR¹¹ is available at <http://www.projects.science.uu.nl/iceclimate/models/greenland.php>. While information on SMB is available from ref. 10. To model ice discharge we use ice discharge estimates from ref. 21.

Code availability. Data analyses have been performed using the SOCET SET 5.6 software package (written by BAE Systems), ArcGIS10.1 (written by Esri Inc.), and custom-built routines for Python, Matlab and Fortran. The codes are not available.

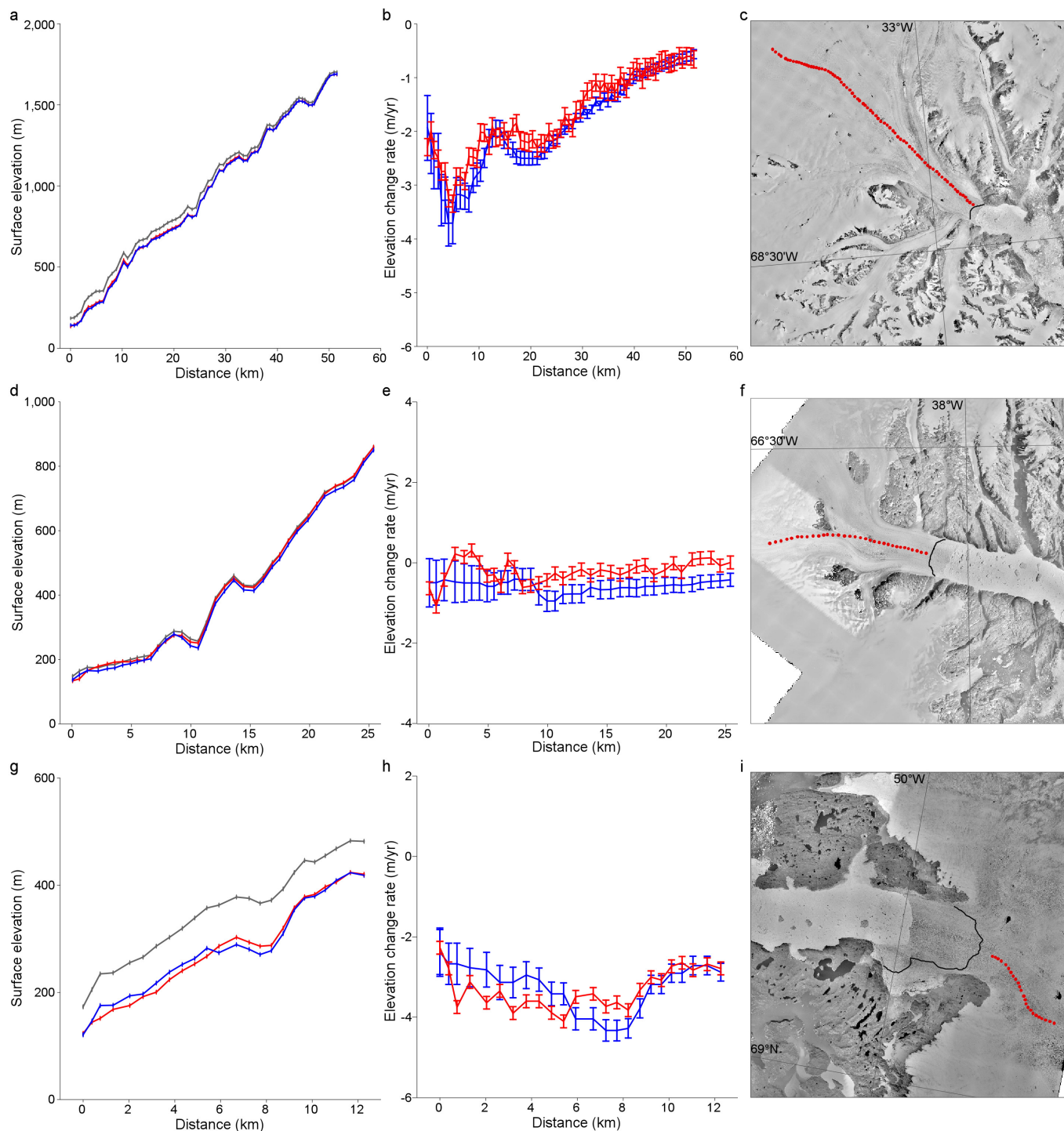
31. Glasser, N. F., Harrison, S., Jansson, K. N., Anderson, K. & Cowley, A. Global sea-level contribution from the Patagonian Icefields since the Little Ice Age maximum. *Nature Geosci.* **4**, 303–307 (2011).
32. Carrivick, J. L., Davies, B. J., Glasser, N. F., Nývlt, D. & Hambrey, M. J. Late-Holocene changes in character and behaviour of land-terminating glaciers on James Ross Island, Antarctica. *J. Glaciol.* **58**, 1176–1190 (2012).
33. Cuffey, K. M. & Paterson, W. S. B. *The Physics of Glaciers* (Elsevier, 2010).
34. Rignot, E. & Mouginot, J. Ice flow in Greenland for the International Polar Year 2008–2009. *Geophys. Res. Lett.* **39**, L11501 (2012).
35. Krabill, W. B. *IceBridge ATM L2 Lcessn Elevation, Slope, and Roughness, [2003–2010] data set* <http://nsidc.org/data/blatm2> (National Snow and Ice Data Center, 2014).
36. Zwally, H. J. et al. *GLAS/ICESat L2 Antarctic and Greenland Ice Sheet Altimetry Data V031 data set* <https://nsidc.org/data/icesat/data.html> (National Snow and Ice Data Center, 2011).
37. National Snow and Ice Data Center. *ICESat: Description of Data Releases data set* http://nsidc.org/data/icesat/data_releases.html (2011).
38. Howat, I. M., Smith, B. E., Joughin, I. R. & Scambos, T. A. Rates of southeast Greenland ice volume loss from combined ICESat and ASTER observations. *Geophys. Res. Lett.* **35**, L17505 (2008).
39. Pritchard, H. D., Arthern, R. J., Vaughan, D. G. & Edwards, L. A. Extensive dynamic thinning on the margins of the Greenland and Antarctic ice sheets. *Nature* **461**, 971–975 (2009).

40. Blair, B. & Hofton, M. *IceBridge LVIS L2 Geolocated Ground Elevation and Return Energy Quartiles, [2010] data set*. <http://nsidc.org/data/ilvis2.html> (National Snow and Ice Data Center, 2010).
41. Ewert, H., Groh, A. & Dietrich, R. Volume and mass changes of the Greenland ice sheet inferred from ICESat and GRACE. *J. Geodyn.* **59–60**, 111–123 (2012).
42. Kjeldsen, K. K. *et al.* Improved ice loss estimate of the northwestern Greenland ice sheet. *J. Geophys. Res. Solid Earth* **118**, 698–708 (2013).
43. Smith, B. E., Fricker, H. A., Joughin, I. R. & Tulaczyk, S. An inventory of active subglacial lakes in Antarctica detected by ICESat (2003–2008). *J. Glaciol.* **55**, 573–595 (2009).
44. Rignot, E. & Kanagaratnam, P. Changes in the velocity structure of the Greenland Ice Sheet. *Science* **311**, 986–990 (2006).
45. Arendt, A. *et al.* *Randolph Glacier Inventory—A Dataset of Global Glacier Outlines Version 3.2*, <http://www.glims.org/RGI/> (Global Land Ice Measurements from Space, 2013).
46. Danish Geodata Agency. *Ground control for 1:150,000 scale aerials, Greenland* <http://gst.dk/emner/landkort-topografi/groenland/ground-control-greenland/> (GST, 2013).
47. Nuth, C. & Kääb, A. Co-registration and bias corrections of satellite elevation data sets for quantifying glacier thickness change. *Cryosphere* **5**, 271–290 (2011).
48. Kääb, A. *Remote Sensing of Mountain Glaciers and Permafrost Creep. Schriftenreihe Physische Geographie* (Univ. Zürich, Department of Geography, 2005).
49. Wang, W., Li, J. & Zwally, H. J. Dynamic inland propagation of thinning due to ice loss at the margins of the Greenland ice sheet. *J. Glaciol.* **58**, 734–740 (2012).
50. Krabill, W. B. *et al.* Greenland Ice Sheet: increased coastal thinning. *Geophys. Res. Lett.* **31**, L24402 (2004).
51. Sasgen, I. *et al.* Timing and origin of recent regional ice-mass loss in Greenland. *Earth Planet. Sci. Lett.* **333–334**, 293–303 (2012).
52. Hurkmans, R. T. W. L. *et al.* Time-evolving mass loss of the Greenland Ice Sheet from satellite altimetry. *Cryosphere* **8**, 1725–1740 (2014).
53. Lecavalier, B. S. *et al.* Revised estimates of Greenland ice sheet thinning histories based on ice-core records Greenland. *Quat. Sci. Rev.* **63**, 73–82 (2013).
54. Pfeffer, W. T., Meier, M. F. & Illangasekare, T. H. Retention of Greenland runoff by refreezing: implications for projected future sea level change. *J. Geophys. Res.* **96**, 22117–22124 (1991).
55. Box, J. E. *et al.* Greenland ice sheet mass balance reconstruction. Part I: Net snow accumulation (1600–2009). *J. Clim.* **26**, 3919–3934 (2013).
56. Andersen, M. L. *et al.* Basin-scale partitioning of Greenland ice sheet mass balance components (2007–2011). *Earth Planet. Sci. Lett.* **409**, 89–95 (2015).
57. Weidick, A. Historical fluctuations of calving glaciers in South and West Greenland. *Rapp. Grønlands Geol. Unders.* **161**, 73–79 (1994).
58. Weidick, B. A. Neoglacial glaciations around Hans Tausen Iskappe, Peary Land, North Greenland. *Medd. Grøn. Geosci.* **39**, 5–26 (2001).



Extended Data Figure 1 | The dh calculation scheme. **a**, Three simulated ice surface profiles based on Glen's flow law, each representing time steps t1 (blue dots), t2 (red dots), and t3 (black dots). **b**, The same profiles as in **a** supplemented with the predicted profile h_{pre_t3} (grey line) derived using an S value of 2.2. The figure shows agreement between the profile h_{t3} and h_{pre_t3} ; hence, if we know the elevation change during one period (for example, t1 and t2), then it is possible to obtain the elevation change during another period (for example, t1 and t3) by multiplying with a constant S . **c**, The elevation changes between t1 and t2 (dh_{t1t2} , blue line) and between t1 and t3 (dh_{t1t3} , brown line). The black dots are the elevation changes between t1 and the predicted surface profile h_{pre_t3} derived using the elevation change between t1 and t2 and an S value of 2.2. The predicted difference

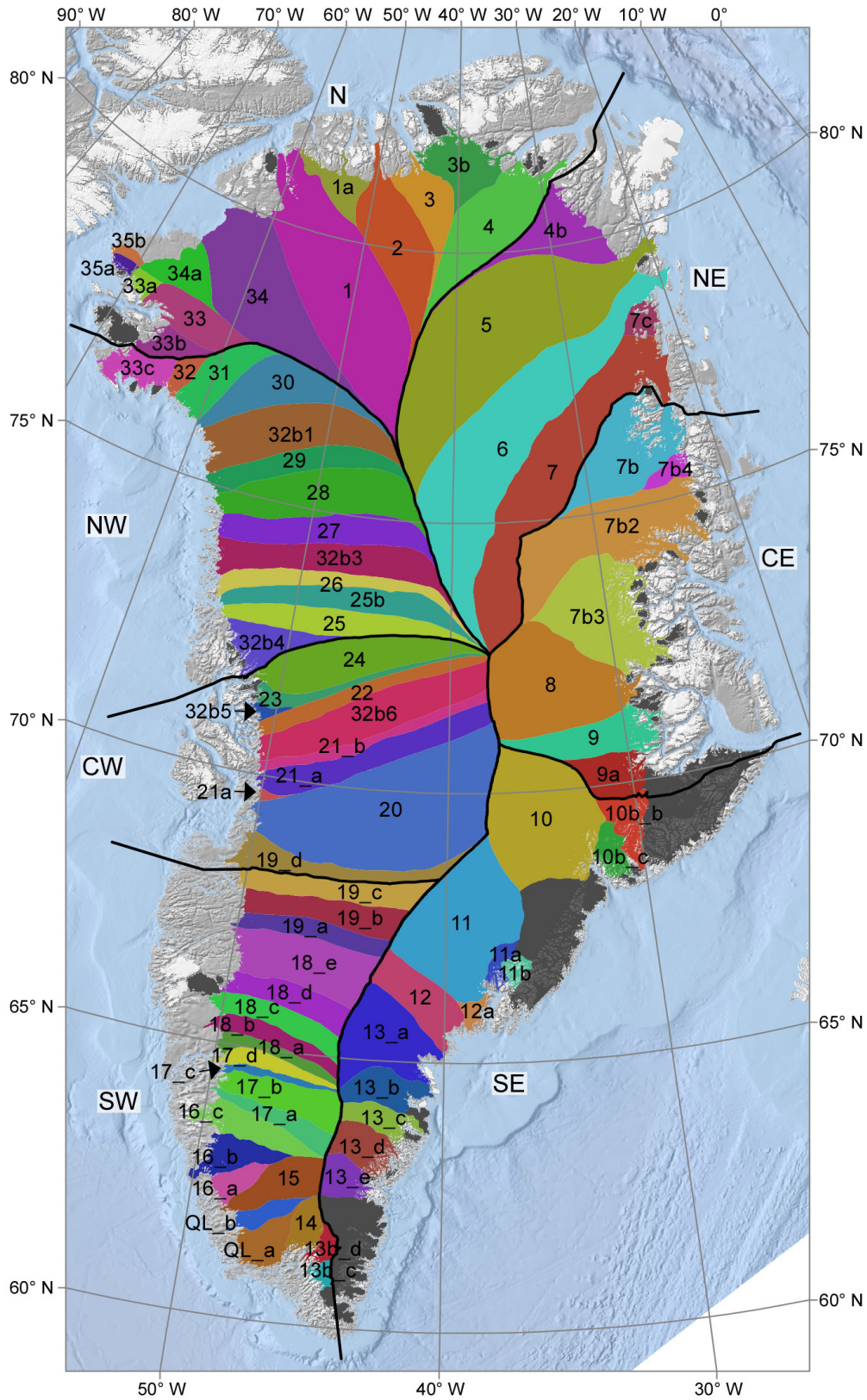
(dh_{t1t3_pre}) between t1 and t3 is derived from dh_{t1t2} and a constant, implying that the surface profile at t1 is part of both the input and of the output. **d**, dh_{t1t2} (blue line), the elevation changes between t3 and t4 (dh_{t3t4} , dark green line), and the predicted dh_{t3t4} (dh_{t3t4_pre} , black dots), which is derived using dh_{t1t2} and an S value of 1.2; thus none of the ice surface profiles are part of both the input and output. If both dh_{t1t2} and dh_{t3t4} are known then S can be derived as the ratio between the observations. **e**, The uncertainty between the profile h_{t3} and h_{pre_t3} using a constant S . Generally the differences are small, though they increase near the margin. **f**, The elevation change between two time steps as a function of elevation. Changes are largest at lower elevation and become close to 0 at $h > 2,500$ m.



Extended Data Figure 2 | Validation of the scaling approach.

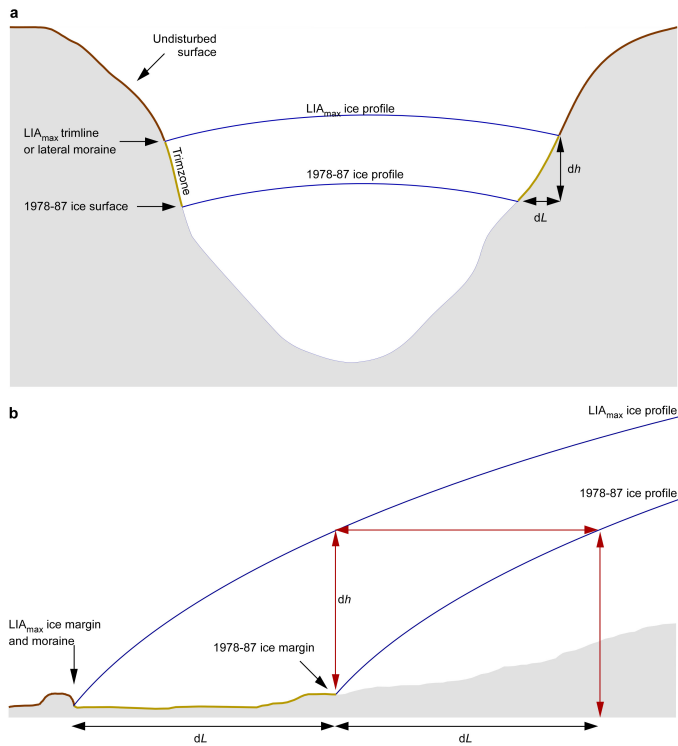
a, Elevation profiles of Kangerlussuaq Glacier in southeast Greenland from the 1981 DEM (grey line), 2003 ATM data (red line), and the predicted surface profile (blue line) in 2003, derived using the scaling approach based on local scale values and the 2003–2010 elevation changes (dh_{solid}). (For a more complete description of the approach using observations see Methods section ‘LIA_{max} to 1978–87 mass balance’). **b**, The elevation change rate between the observed 2003 surface profile (red) and the predicted 2003 surface profile (blue) relative to the 1981 DEM. The blue vertical lines denote uncertainty estimates that include an uncertainty related to the scaling approach, an error related to observed changes during 2003–2010, and an uncertainty related to the scaling of point-based observations. The red vertical lines denote an uncertainty associated with

the observed elevation changes during 1981–2003 and includes combined errors of the measured height derived from stereo photogrammetric DEM and 2003 ATM data. **c**, A 1981 orthophoto of Kangerlussuaq Glacier with 2003 ATM data (red dots) and the May 2003 glacier front (black line). **d–f** and **g–i** illustrate the same as **a–c** for Helheim Glacier and Jakobshavn Isbræ, respectively. However, for Jakobshavn Isbræ the DEM and orthophoto is from 1985. Note the different scales for each of the glaciers. Comparing the elevation change rates derived from the scaling approach and those directly from the observations, we find good agreement as the error bars overlap. Thus, we regard the illustrated comparison as a validation of our method of deriving ice-sheet-wide mass balance estimates.

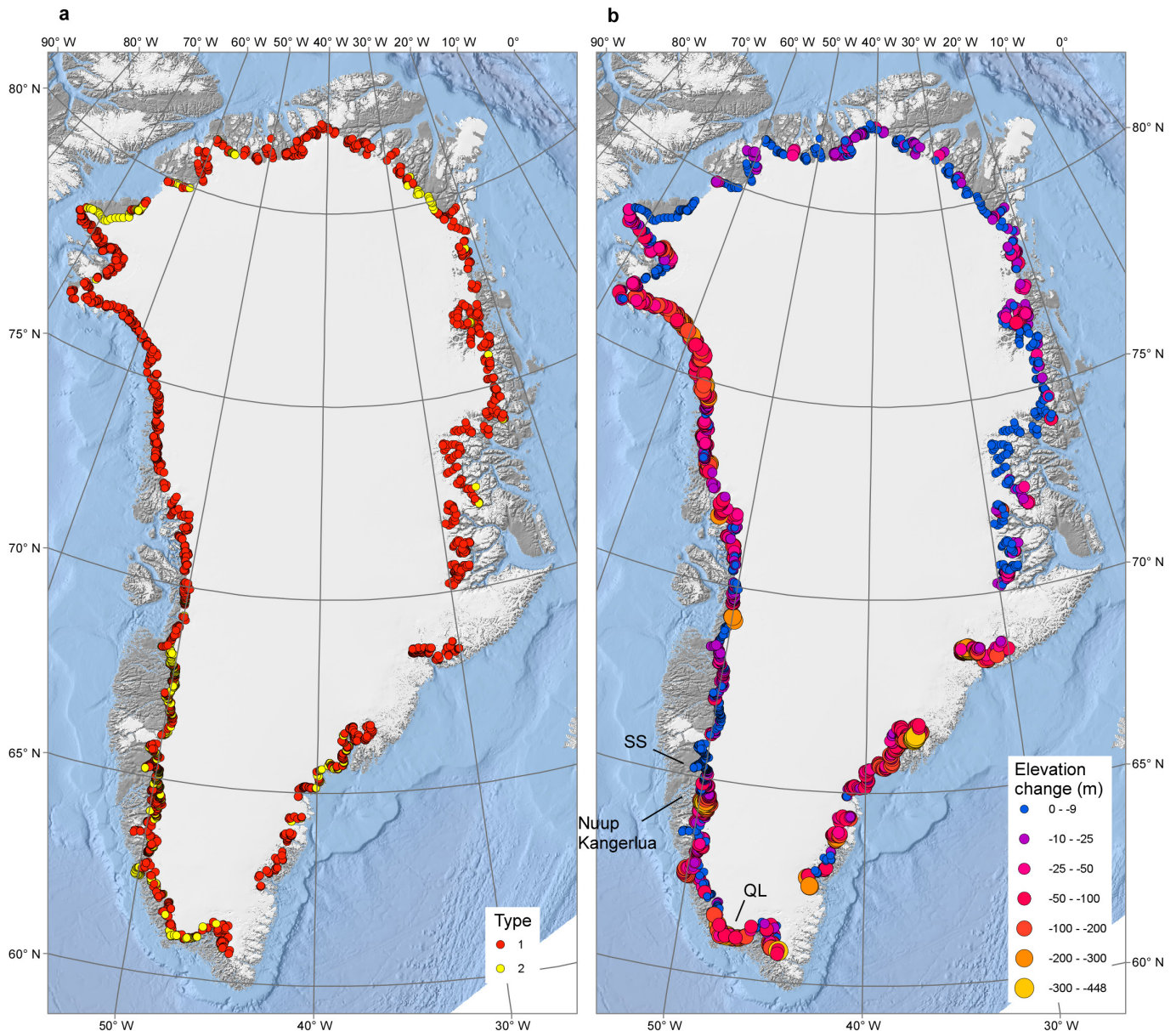


Extended Data Figure 3 | GIS calculation basin subdivision. Calculation basins modified from ref. 44 to include slower-moving areas of the ice sheet. Note that three areas on the southeast coast have been omitted due to an insufficient number of LIA to 1978–87 data points caused by

extensive snow cover on the vertical images. The total ice mask covers 1,647,907 km². The additional areas included in the ice mask used by ref. 18 are shown in dark grey and in total the ice mask covers 1,739,564 km².



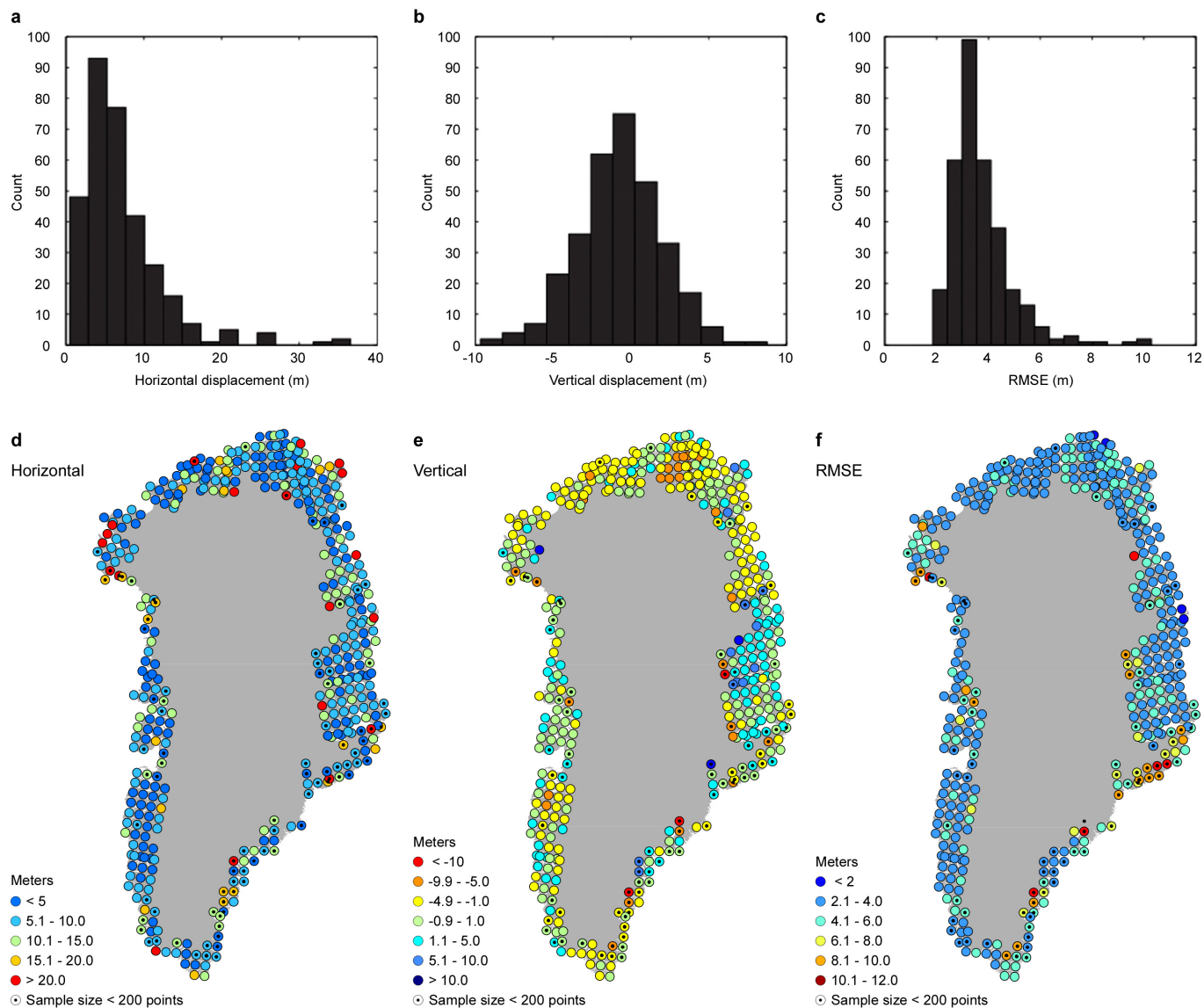
Extended Data Figure 4 | Mapping elevation changes during LIA_{max} to 1978-87. **a**, Type 1 points are placed at the trimline or lateral moraine marking the LIA_{max} position and at the 1978-87 ice surface perpendicular to the flow direction, and as we assume that the cross-section profile of the glacier is the same during the LIA_{max} and 1978-87 then the vertical difference dh is the thinning at this location. This approach is the same as used by ref. 9. **b**, For Type 2 points we assume that the longitudinal shape of the glacier is the same during the LIA_{max} as in 1978-87. Points are placed at the LIA_{max} margin and at the 1978-87 margin, and assuming a longitudinal profile that does not change over time, the distance dL is used to find the vertical difference between the 1978-87 point and a point on the glacier at a distance of dL following the same flowline. Points for glaciers receding on steep slopes have been discarded.



Extended Data Figure 5 | Distribution and values of dh_{LIA} points.

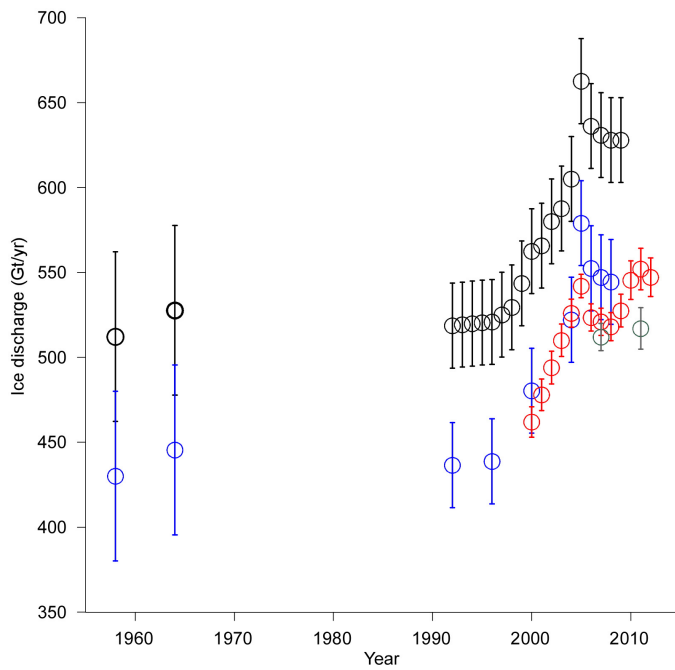
a, Distribution of the two point types used to determine thinning between LIA_{max} and 1978–87. **b**, From the type 1 and type 2 points, net elevation change dh_{LIA} is measured based on 3,003 point measurements from the LIA_{max} to 1978–87. Of the 3,003 pairs—that is, 6,006 point measurements—2,476 are measured as type 1 and 527 are type 2. The majority of the type 2 points are found along the land-terminating and slower-moving parts of the ice sheet, whereas type 1 points are found in valleys through which the ice flows and on nunataks. dh_{LIA} values range between zero and -448 m (a negative value implies thinning). The largest dh_{LIA} values are found along the major marine-outlet glaciers along the northwest and southeast coast and along the rim of the Qassimiuq lobe (QL), while in contrast the lower dh_{LIA} values are found along the slower-moving margins of the typically land-terminating ice sheet. In some areas around the ice sheet no trimlines are visible and/or the ice margin is in contact with the LIA moraines. Analysis of glacier front positions for outlet glaciers in the north, central west, southwest, and south using historical aerial photographs from the 1930s and onwards^{15,57,58} suggest

that a few outlet glaciers, primarily land-terminating, have been stable or advanced since the LIA. In the northwest, central west, and southwest snow cover on the 1978–87 vertical aerial images is generally limited, which eases the distinction between freshly eroded bedrock, newly deposited glacial sediment, and non-eroded vegetated terrain surfaces. This supports the notion that if no trimline is visible on the photographs, then the ice margin is at an advanced and stable stage. Hence, the dh_{LIA} and dL_{LIA} values for points are zero. An example of a glacier that has advanced during the twentieth century is the Saqqap Sermia (SS)⁵⁷ in the Nuup Kangerlua (Godthåbsfjord) complex in southwest Greenland. Here no trimlines are visible along the valley and the boundary between ice and vegetation cover is only interrupted by small meltwater channels, and at the glacier front no end moraines are visible on the meltwater plain. In the present setup we are not able to assign any post-LIA mass gain; however, as only a limited number of outlet glaciers have advanced and exceeded the LIA front position during the twentieth century we regard this mass gain as negligible relative to the ice-sheet-wide mass loss.



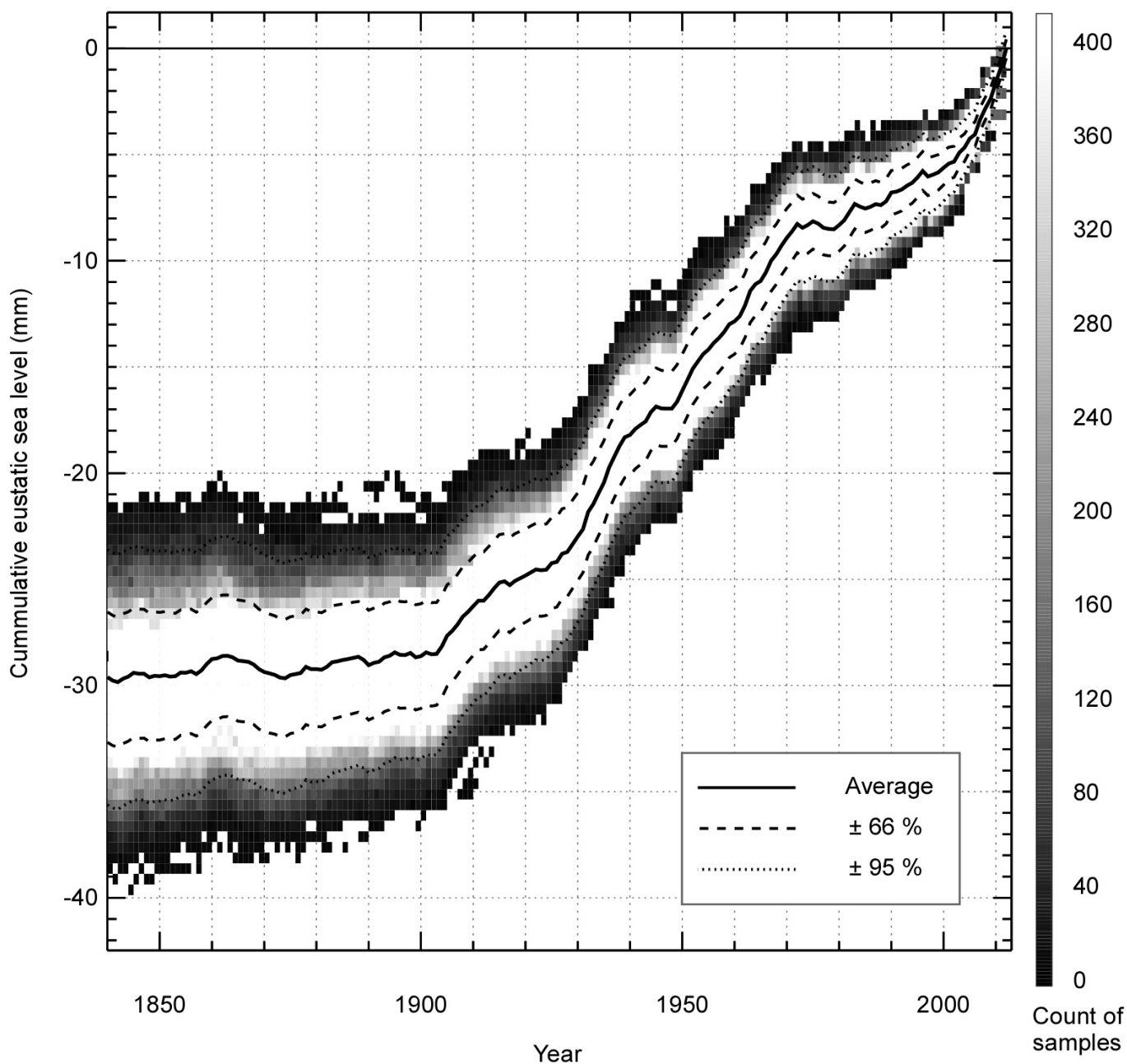
Extended Data Figure 6 | Horizontal and vertical displacements in aero-photogrammetric DEM. a–c, Histograms of the horizontal (a) and vertical (b) co-registration displacements for each 50 km × 50 km grid cell show that the aero-photogrammetric DEM compilation is generally accurate to within 10 m horizontally and 6 m vertically with a precision greater than 4 m (1σ confidence level) (c). d–f, The horizontal

(d) and vertical (e) components of the co-registration vectors between 50 km × 50 km sections of the aero-photogrammetric DEM compilation and ICESat laser altimetry are plotted with the root-mean-square error of stable terrain differences after adjusting for the three-dimensional mis-registration (f).



Extended Data Figure 7 | Estimates of ice-sheet-wide iceberg discharge.

Ice discharge estimates and associated errors (vertical bars) from ref. 24 (black), ref. 3 (blue), ref. 21 (red), and ref. 56 (grey). We note that the used discharge estimates of ref. 21 are 15 Gt yr^{-1} greater than those of ref. 56, 30 Gt yr^{-1} less than those of ref. 3, and 110 Gt yr^{-1} less than those of ref. 24. Such discrepancies are attributed to differences in data availability and assumptions used for filling gaps or the method used to correct for SMB between the inland flux gates and the grounding lines²¹.



Extended Data Figure 8 | Temporal variability of the mass balance expressed as cumulative eustatic sea level rise. Reconstructed temporal mass balance during the period 1840–2012 derived using revised SMB

estimates from ref. 10 and modelled ice discharge, calculated as a function of six-year average runoff. The uncertainty is assessed from a Monte Carlo simulation using 4,000 samples for each year.